



The relativistic pulsar–white dwarf binary PSR J1738+0333 – II. The most stringent test of scalar–tensor gravity

Paulo C. C. Freire,¹★ Norbert Wex,¹ Gilles Esposito-Farèse,² Joris P. W. Verbiest,¹ Matthew Bailes,³ Bryan A. Jacoby,⁴ Michael Kramer,^{1,5} Ingrid H. Stairs,⁶ John Antoniadis¹† and Gemma H. Janssen⁵

¹Max-Planck-Institut für Radioastronomie, Auf dem Hügel 69, D-53121 Bonn, Germany

²UPMC-CNRS, UMR7095, Institut d’Astrophysique de Paris, GReCO, 98bis boulevard Arago, F-75014 Paris, France

³Centre for Astrophysics and Supercomputing, Swinburne University of Technology, PO Box 218, Hawthorn, VIC 31122, Australia

⁴The Aerospace Corporation, 15049 Conference Center Drive, Chantilly, VA 20151-3824, USA

⁵University of Manchester, Jodrell Bank Centre for Astrophysics, Alan Turing Building, Manchester M13 9PL

⁶Department of Physics and Astronomy, University of British Columbia, 6224 Agricultural Road, Vancouver, BC V6T 1Z1, Canada

Accepted 2012 May 4. Received 2012 May 4; in original form 2012 February 28

ABSTRACT

We report the results of a 10-year timing campaign on PSR J1738+0333, a 5.85-ms pulsar in a low-eccentricity 8.5-h orbit with a low-mass white dwarf companion. We obtained 17 376 pulse times of arrival with a stated uncertainty smaller than 5 μs and weighted residual rms of 1.56 μs. The large number and precision of these measurements allow highly significant estimates of the proper motion $\mu_{\alpha,\delta} = (+7.037 \pm 0.005, +5.073 \pm 0.012) \text{ mas yr}^{-1}$, parallax $\pi_x = (0.68 \pm 0.05) \text{ mas}$ and a measurement of the apparent orbital decay, $\dot{P}_b = (-17.0 \pm 3.1) \times 10^{-15} \text{ s s}^{-1}$ (all 1σ uncertainties). The measurements of $\mu_{\alpha,\delta}$ and π_x allow for a precise subtraction of the kinematic contribution to the observed orbital decay; this results in a significant measurement of the intrinsic orbital decay: $\dot{P}_b^{\text{Int}} = (-25.9 \pm 3.2) \times 10^{-15} \text{ s s}^{-1}$. This is consistent with the orbital decay from the emission of gravitational waves predicted by general relativity, $\dot{P}_b^{\text{GR}} = -27.7^{+1.5}_{-1.9} \times 10^{-15} \text{ s s}^{-1}$, i.e. general relativity passes the test represented by the orbital decay of this system. This agreement introduces a tight upper limit on dipolar gravitational wave emission, a prediction of most alternative theories of gravity for asymmetric binary systems such as this. We use this limit to derive the most stringent constraints ever on a wide class of gravity theories, where gravity involves a scalar-field contribution. When considering general scalar–tensor theories of gravity, our new bounds are more stringent than the best current Solar system limits over most of the parameter space, and constrain the matter–scalar coupling constant α_0^2 to be below the 10^{-5} level. For the special case of the Jordan–Fierz–Brans–Dicke, we obtain the 1σ bound $\alpha_0^2 < 2 \times 10^{-5}$, which is within a factor of 2 of the Cassini limit. We also use our limit on dipolar gravitational wave emission to constrain a wide class of theories of gravity which are based on a generalization of Bekenstein’s Tensor–Vector–Scalar gravity, a relativistic formulation of modified Newtonian dynamics.

Key words: gravitation – gravitational waves – pulsars: individual: PSR J1738+0333.

1 INTRODUCTION

Pulsar J1738+0333 is one of seven recycled pulsars discovered in a high-Galactic latitude ($15^\circ < |b| < 30^\circ$, $-100^\circ < l < 50^\circ$) Parkes multi-beam pulsar survey (Jacoby 2005; Jacoby et al. 2007). It has

a spin period P of 5.85 ms and it is located in a low-eccentricity ($e < 4 \times 10^{-7}$) binary system with an orbital period (P_b) of 8.5 h; the projected semi-major axis of the pulsar orbit (x) is 0.3434 light seconds. The Parkes timing determined a phase-coherent timing solution with precise spin, orbital and astrometric parameters that allowed the detection of the companion of the pulsar at optical wavelengths (Jacoby 2005).

The results of the optical observations of the companion are described in detail by Antoniadis et al. (2012, hereafter Paper I); it is a white dwarf (WD), and from its spectrum they estimate its mass

*E-mail: pfreira@mpifr-bonn.mpg.de

†Member of the International Max Planck Research School (IMPRS) for Astronomy and Astrophysics at the Universities of Bonn and Cologne.

$M_c = 0.181^{+0.008}_{-0.007} M_\odot$ (1σ , where M_\odot represents one solar mass; we also define $m_c \equiv M_c/M_\odot$). The paper also presents measurements of the Doppler shifts of the WD spectral lines, which are used to estimate the systemic radial velocity $\gamma = (-42 \pm 16) \text{ km s}^{-1}$ and the semi-amplitude of the WD orbital velocity projected along the line of sight $K_c = (171 \pm 5) \text{ km s}^{-1}$, consistent (but significantly more precise) with the value obtained by Jacoby (2005), $K_c = (181 \pm 27) \text{ km s}^{-1}$. This measurement is combined with its pulsar equivalent $K_p = 2\pi c P_b = 21.10336 \text{ km s}^{-1}$ to estimate the mass ratio: $q \equiv M_p/M_c = K_c/K_p = 8.1 \pm 0.2$. Given M_c , this implies a pulsar mass $M_p = 1.46^{+0.06}_{-0.05} M_\odot$. Finally, from Kepler's laws they derive an orbital inclination $i = 32.6 \pm 1.0^\circ$.

The position of PSR J1738+0333 makes it detectable with the Arecibo Observatory's 305-m William E. Gordon radio telescope, which provides about 15 times the sensitivity of the Parkes telescope and therefore allows much more precise timing. Regular Arecibo observations of PSR J1738+0333 started in 2003. Given the mass measurements obtained from the optical/radio data, and the knowledge that $e < 4 \times 10^{-7}$, general relativity (GR) predicts an orbital decay of $\dot{P}_b^{\text{GR}} = (-27.7^{+1.5}_{-1.9}) \times 10^{-15} \text{ s s}^{-1}$ (henceforth fs s^{-1}) due to the emission of gravitational waves (GW). Our early simulations suggested that using Arecibo we would be able to measure this effect within a few years.

The organization of the remainder of this paper is as follows. In Section 2 we describe in detail the observations and how the pulse times of arrival and the timing solution were derived. In Section 3 we discuss the detection of the orbital decay of the system. We compare it with the prediction from GR, and derive an upper limit for any excess GW emission. In Section 4, we use this limit to derive an upper limit for the emission of dipolar GWs. In the following sections, we discuss the implications of this result for alternative theories of gravity, specifically in Section 5 for tensor–scalar theories of gravity and in Section 6 for a class of tensor–vector–scalar (TeVeS) theories of gravity similar to the theory proposed by Bekenstein (2004), which is a relativistic formulation of the modified Newtonian dynamics (MOND) proposed by Milgrom (1983). Finally, in Section 7, we summarize our results and highlight the prospects opened by continued timing of this system.

2 RADIO TIMING OBSERVATIONS

2.1 Observational setup and data reduction

PSR J1738+0333 was discovered with the 64-m Parkes telescope in an observation taken in 2001. We started timing it regularly on 2001 September 26 using the 21-cm multi-beam receiver system and the $2 \times 512 \times 0.5 \text{ MHz}$ filterbank. The Parkes datataking and processing are described in detail in Jacoby (2005).

In 2003 August we started regular observations of this MSP using the L-wide receiver of the 305-m William E. Gordon Telescope at the Arecibo Observatory and the Wide-band Arecibo Pulsar Processors (WAPPs) to process the signal. The WAPPs are general-purpose auto-correlators capable of processing a band of up to 100 MHz each (Dowd, Sisk & Hagen 2000). First, they digitize the incoming voltages as three-level values. The machine then calculates the auto-correlation function (ACF) for a specified number of time lags, in our case 256. These are integrated for a time t_s of $64 \mu\text{s}$, after which they are written to disk as 16-bit integers for later off-line analysis. The four WAPPs were centred at frequencies F of 1170, 1310, 1410 and 1510 MHz.

The ACFs from the WAPPs are, later on, read from disk during off-line processing. First, they are Fourier transformed using Duncan Lorimer's SIGPROC routine 'filterbank', producing 100-MHz-wide, 256-channel power spectra. To eliminate signal distortions caused by the edges of the WAPP bands we set the values of the lower and higher 16 channels to zero, all other channel values are unchanged. These spectra are then divided into four sub-bands. Each of these is dedispersed at the DM of the pulsar. The resulting time series is then folded modulo the pulsar rotational period, using a polynomial expansion of the pulsar spin phase as a function of time predicted by the best existing ephemeris. For each of these sub-bands, the pulses are integrated for 4 min as single 512-bin pulse profiles. Only on days when the pulsar is consistently faint (the flux density changes because of scintillation caused by the interstellar medium) do we integrate the pulse profiles for 600 s. All of this processing is done using the 'sig_foldpow' routine, written by one of us (IHS). Given the pulsar's dispersion measure (DM; a measurement of the column density of free electrons between the Earth and the pulsar) of $33.77 \text{ cm}^{-3} \text{ pc}$, the dispersive smearing per channel (with bandwidth $\delta F = 100 \text{ MHz}/256 = 0.390625 \text{ MHz}$) was $t_{\text{DM}} = 8.3 \mu\text{s}$ ($\text{DM}/\text{cm}^{-3} \text{ pc})(\delta F/\text{MHz})(F/\text{GHz})^{-3} = 68.3, 48.7, 39.0$ and $31.8 \mu\text{s}$ per channel, respectively. The total time resolution $dt = \sqrt{t_s^2 + t_{\text{DM}}^2}$ was therefore $93.6, 80.4, 75.0$ and $71.5 \mu\text{s}$, respectively.

Producing a large number of such profiles has many advantages: (a) the separation in frequency allows the use of polynomial coefficients derived specifically for the radio frequency of each sub-band in such a way that the orbital phase of the binary is constant for the pulse arrival time at each frequency, not constant for a particular time. This is very important for systems with short orbital periods like PSR J1738+0333, where the difference in arrival times at the lower and upper edges of the band caused by dispersion by the ionized interstellar medium corresponds to a non-negligible shift in the orbital phase. (b) The production of many TOAs in time preserves the important orbital information contained in them. (c) By having small bandwidths and integration times, we minimize profile smearing due to imperfections in the ephemeris and DM model. Finally, (d) we take full advantage of the power of scintillation – in some occasions, the signal-to-noise ratio in a $25 \text{ MHz} \times 4\text{-min}$ subsection is larger than for the whole observation.

2.2 Derivation of times of arrival

The best pulse profile, resulting from more than 1 h of data, is displayed in Fig. 1. The narrow central component is the cause of the excellent timing precision for this pulsar. This profile does not show significant changes with radio frequency beyond what one should expect from the change in time resolution of the system dt with frequency. For this reason, the best profile is then cross-correlated with *all* the 4-min/25 MHz pulse profiles in the Fourier domain (Taylor 1992); the phase offset that yields the best match is used to derive the time of arrival (TOA) of a particular pulse (normally that closest to the start of each sub-integration) measured at the local (topocentric) time frame. In total we obtain 17376 TOAs from Arecibo data. The previous number of Parkes measurements is 100.

We carry out subsequent TOA analysis using the TEMPO2 software package (Edwards, Hobbs & Manchester 2006; Hobbs, Edwards & Manchester 2006). This uses the clock corrections intrinsic to the observatory, the Earth rotation data and the observatory coordinates to convert the topocentric TOAs to Terrestrial Time (TT), as

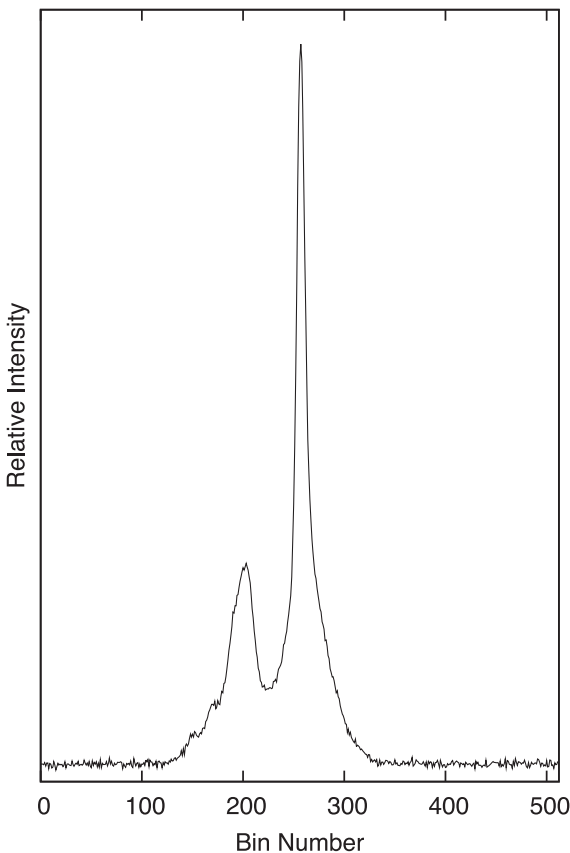


Figure 1. PSR J1738+0333 average pulse profile at 1400 MHz taken with the WAPP spectrometers. A full 512-bin rotation cycle is displayed.

maintained by the Bureau International des Poids et Mesures. From these TEMPO2 derives arrival times at the Solar system Barycentre using the position of the Observatory that is calculated using the DE/LE 421 Solar system ephemeris (Folkner, Williams & Boggs 2008); for details see Edwards et al. (2006). These, like our timing parameters, are expressed in Barycentric Coordinate Time (TCB).

With the correct rotation count, TEMPO2 can vary the timing parameters in order to minimize the difference between the observed and predicted barycentric TOAs (the timing residuals). The residuals are weighted according to the estimated uncertainty of each TOA. The resulting set of timing parameters constitutes a preliminary phase-coherent timing solution (an ‘ephemeris’). If the TOA uncertainties are underestimated, or if there are systematics present in the data, the reduced χ^2 of the fit will be larger than 1. For this preliminary ephemeris, the reduced χ^2 is 2.05, which, as we show below, is mostly caused by variations in the intervening electron column density.

The main advantage of having WAPP search data stored on disk and doing the analysis off-line is that it allows for iterative improvement of the pulsar ephemeris; this process is particularly important at the earlier stages when the ephemeris is not yet very precise. With each improved ephemeris, we dedispersed and folded the data again, obtaining pulse profiles with improved signal-to-noise ratio, which are then used to derive better TOAs that further improve the ephemeris. This avoids orbital phase-dependent smearing of the pulse profiles and the creation of orbital phase-dependent timing artefacts, which can corrupt the determination of orbital parame-

ters, particularly the orbital phase and orbital period variation (Nice, Stairs & Kasian 2008).

At the early stages of our timing programme, we checked the timing accuracy of the WAPPs by making a few simultaneous observations with the Arecibo Signal Processor (ASP). The ASP is a real-time coherent dedispersion system implemented in software, which can process 64 MHz of baseband signal (Demorest 2007) and is known to provide very stable timing. No significant differences in the timing of the two back-ends was found; this implies that, within measurement precision, the WAPP timing is accurate.

2.3 DM variations and the timing model

The preliminary ephemeris described above assumes a constant DM. As we can see in the right-hand plot of Fig. 2, this ephemeris describes the TOAs rather poorly, with large trends in the post-fit residuals. These are especially noticeable once we calculate daily residual averages.

We used this preliminary ephemeris to measure the pulsar’s DM for each day of observations. This is only possible because of the wide band of the L-wide receiver at Arecibo – from 1120 to 1730 MHz, of which we used the cleanest parts, 1120–1220 and 1260–1560 MHz. The results of these measurements are presented in the left-hand plot of Fig. 2. The DM varies significantly with time, and its variation correlates with the daily residual averages; this implies that the latter must, to a large extent, be caused by the former. They have amplitudes of the order of $0.002 \text{ cm}^{-3} \text{ pc}$, which cause extra dispersive delays of the order of 4 μs , and a dominant time-scale of the order of a few years. This is similar to the time-scales associated with GWs from supermassive black hole binaries. This highlights the importance of accurate and dense multi-frequency TOA measurements and precise DM corrections when attempting to detect such waves with pulsar timing (Verbiest et al. 2009).

These DM variations cannot be described by a simple linear variation with time. For this reason, we included eight DM derivatives in our definitive timing model, which is presented in Table 1; the uncertainties were derived by TEMPO2 except where stated otherwise. This DM model describes the daily DM measurements very well (see the left-hand plot of Fig. 2), but is only valid within the time interval for which we have significant multi-frequency data, i.e. since the start of the Arecibo observations in 2003. The predicted values start diverging fast outside this range, but this does not affect the results discussed in this paper. This method has the benefit that any possible correlations of the coefficients of the DM model with the timing parameters are taken into account, leading to more conservative (and in our opinion more realistic) estimates of the parameter uncertainties.

This ephemeris describes the TOAs much better than the preliminary ephemeris, as displayed in the left-hand plot of Fig. 3. However, there are still systematic variations in the daily residual averages; these excursions reach a maximum of about 0.5 μs and have time-scales of a few months to a year. In order to estimate the timing parameters with more realistic uncertainties, we added an uncertainty of 0.5 μs in quadrature to the estimated uncertainty of every TOA.

This rescaling of our errors results in a reduced χ^2 of 1 for short time-scales and 1.02 for the whole data set, suggesting that the uncertainties on the derived parameters are reliable. However, given the systematic nature of these excursions, small systematics on parameters with comparable time-scales (in particular the parallax)

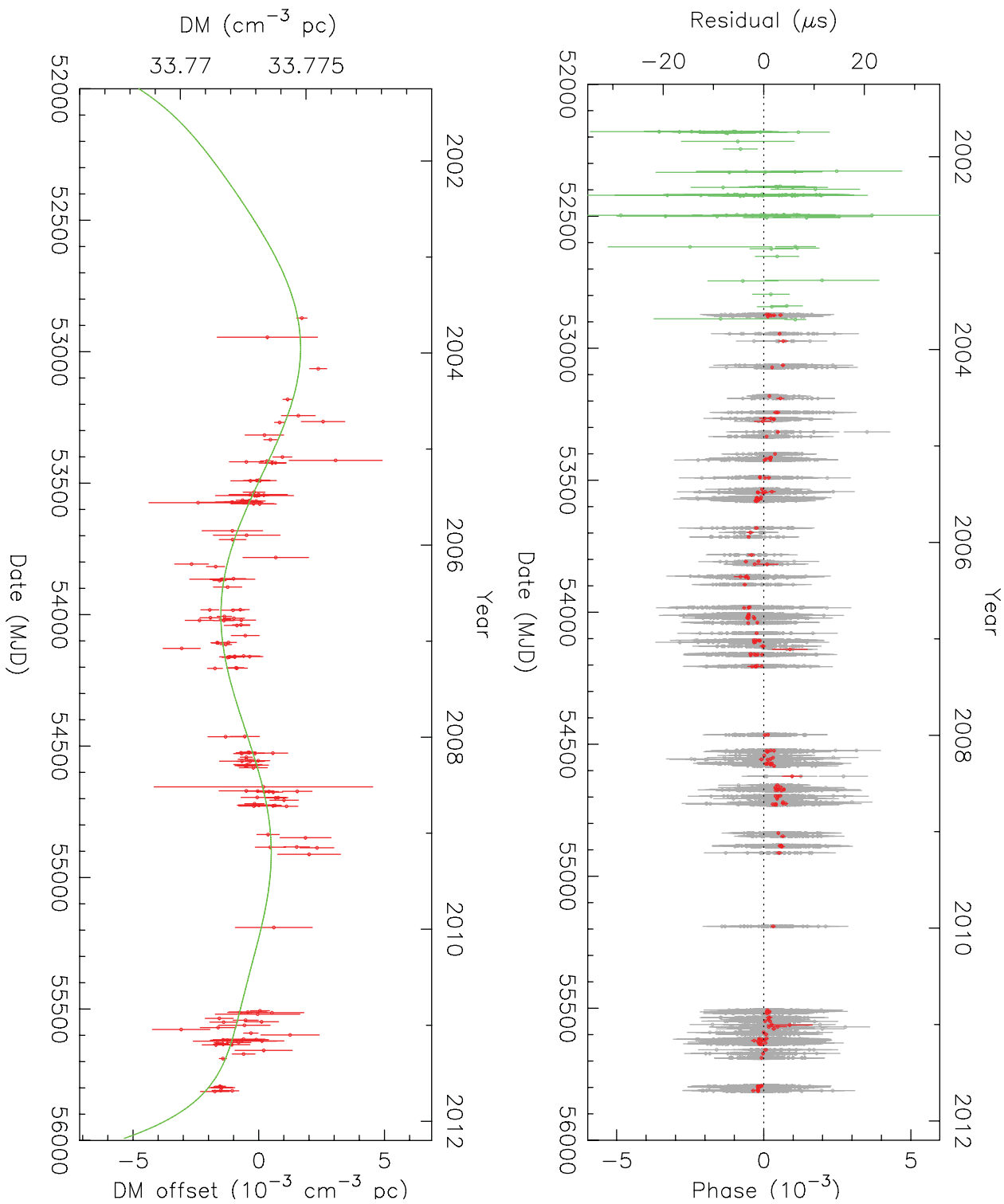


Figure 2. Left-hand plot: daily DM measurements versus time. Given the non-linear variation of the DM, it is clear that it must be modelled using a high-order polynomial. We display in green the eighth-degree polynomial in Table 1; this fits the DM evolution well inside the range where there are DM measurements, but diverges fast outside that range. Right-hand plot: post-fit residuals versus time. The residuals of the Parkes (green) and Arecibo (grey) TOAs were obtained with a preliminary ephemeris that assumes a constant DM. The averages of the residuals for each sidereal day are indicated in red. Notice their similarity with the daily DM averages; this implies that the former are (mostly) caused by the latter.

Table 1. Parameters for the PSR J1738+0333 system. In parentheses we present the 1σ uncertainties in the last digit quoted, as estimated by TEMPO2. If the value and uncertainty are tagged with an (a) then they were derived from a Monte Carlo procedure (Section 3.4). (b) The Shapiro delay parameters r and s were not fitted in the derivation of the timing model; the values used were derived from a combination of other timing and optical parameters (Section 2.4). All timing parameters are derived using TEMPO2 and are displayed as measured at the Solar system Barycentre, in TCB. The ‘test parameters’ were not fitted when deriving the main timing model, but their values were derived fitting for all the other parameters in the model.

<i>Timing parameters</i>	
Reference time (MJD)	54 600.000 177 6275
Right ascension, α (J2000)	17 ^h 38 ^m 53 ^s 965 8386(7)
Declination, δ (J2000)	03° 33' 10" 866 67(3)
Proper motion in α , μ_α (mas yr ⁻¹)	+7.037(5)
Proper motion in δ , μ_δ (mas yr ⁻¹)	+5.073(12)
Parallax, π_x (mas) (a)	0.68(5)
Spin frequency, ν (Hz)	170.937 369 911 463 92(3)
First derivative of ν , $\dot{\nu}$ (fHz s ⁻¹)	-0.704 774(4)
Orbital period P_b (d)	0.354 790 739 8724(13)
Projected semi-major axis, x (lt-s)	0.343 429 130(17)
Time of Ascending Node, T_{asc} (MJD)	54 600.200 400 12(5)
$\eta \equiv e \sin \omega$	(-1.4 ± 1.1) × 10 ⁻⁷
$\kappa \equiv e \cos \omega$	(3.1 ± 1.1) × 10 ⁻⁷
First derivative of P_b , \dot{P}_b (fs s ⁻¹)	-17.0(3.1)
‘Range’ parameter of Shapiro delay, r (μs) (b)	0.8915
‘Shape’ parameter of Sapiro delay, $s \equiv \sin i$ (b)	0.538 77
DM (cm ⁻³ pc)	33.773 12(4)
First derivative of DM, DM1 (cm ⁻³ pc yr ⁻¹)	+0.001 08(3)
DM2 (cm ⁻³ pc yr ⁻²)	-0.000 41(3)
DM3 (cm ⁻³ pc yr ⁻³)	-0.000 279(9)
DM4 (cm ⁻³ pc yr ⁻⁴)	+0.000 059(6)
DM5 (cm ⁻³ pc yr ⁻⁵)	+0.000 0230(19)
DM6 (cm ⁻³ pc yr ⁻⁶)	-0.000 0019(3)
DM7 (cm ⁻³ pc yr ⁻⁷)	-0.000 000 90(11)
DM8 (cm ⁻³ pc yr ⁻⁸)	-0.000 000 060(10)
<i>Test parameters</i>	
First derivative of x , \dot{x} (fs s ⁻¹)	0.7(5)
Second derivative of ν , $\ddot{\nu}$ (10 ⁻²⁸ Hz s ⁻²)	-0.6(2.3)
<i>Optical parameters</i>	
Companion mass, M_c (M _⊕)	0.181 ^{+0.008} _{-0.007}
Spectroscopic companion radius, R_c (R _⊕)	0.037 ^{+0.004} _{-0.003}
Semi-amplitude of orbital velocity of companion, K_c (km s ⁻¹)	171(5)
<i>Derived parameters</i>	
Galactic longitude, l	27°7213
Galactic latitude, b	17°7422
Distance, d (kpc)	1.47(10)
Total proper motion, μ (mas yr ⁻¹)	8.675(8)
Position angle of proper motion, Θ_μ (J2000)	53°72(7)
Position angle of proper motion, Θ_μ (Galactic)	116°12(7)
Spin period, P (s)	0.005 850 095 859 775 683(5)
First derivative of spin period, \dot{P} (10 ⁻²⁰ s s ⁻¹)	2.411 991(14)
Intrinsic \dot{P} , \dot{P}_{int} (10 ⁻²⁰ s s ⁻¹) (a)	2.243(13)
Characteristic age, τ_c (Gyr)	4.1
Transverse magnetic field at the poles, B_0 (10 ⁹ G)	0.37
Rate or rotational energy loss, \dot{E} (10 ³³ erg s ⁻¹)	4.4
Mass function, f (M _⊕)	0.0003455012(11)
Mass ratio, $q \equiv M_p/M_c$	8.1(2)
Orbital inclination, i (°)	32.6(1.0)
Pulsar mass, M_p (M _⊕)	1.46 ^{+0.06} _{-0.05}
Total mass of binary, M_t (M _⊕)	1.65 ^{+0.07} _{-0.06}
Eccentricity, e	(3.4 ± 1.1) × 10 ⁻⁷
Apparent \dot{P}_b due to Shklovskii effect, \dot{P}_b^{Shk} (fs s ⁻¹) (a)	8.2 ^{+0.6} _{-0.5}
Apparent \dot{P}_b due to Galactic acceleration, \dot{P}_b^{Gal} (fs s ⁻¹) (a)	0.58 ^{+0.16} _{-0.14}
Intrinsic \dot{P}_b , \dot{P}_b^{Int} (fs s ⁻¹) (a)	-25.9(3.2)
Predicted \dot{P}_b , \dot{P}_b^{GR} (fs s ⁻¹)	-27.7 ^{+1.5} _{-1.9}
‘Excess’ orbital decay, $\dot{P}_b^{\text{xs}} = \dot{P}_b^{\text{Int}} - \dot{P}_b^{\text{GR}}$ (fs s ⁻¹) (a)	+2.0 ^{+3.7} _{-3.6}
Time until coalescence, τ_m (Gyr)	~ 13.2

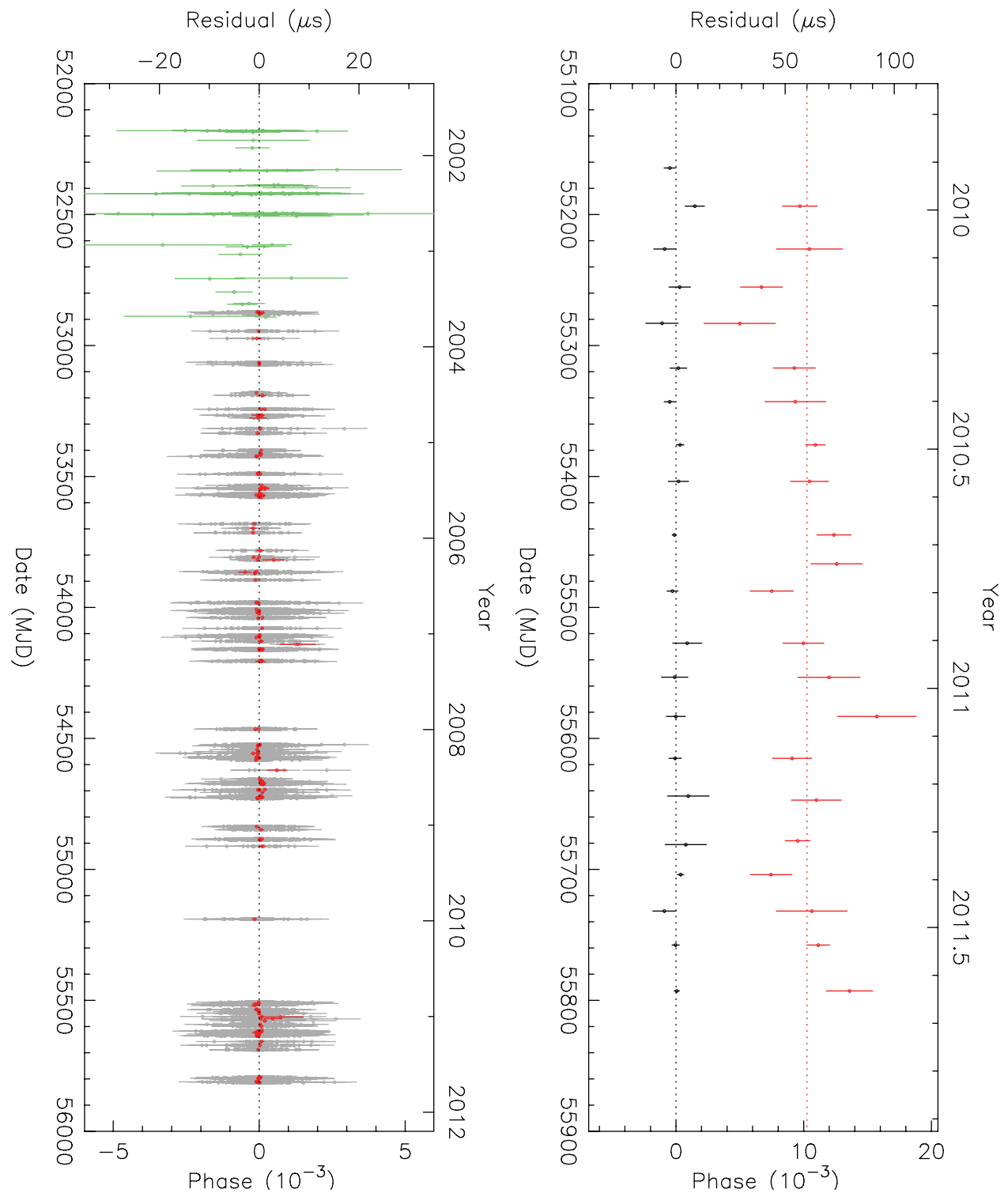


Figure 3. Left-hand plot: post-fit residuals versus time. The residuals of the Parkes (green) and Arecibo (grey) TOAs were obtained with the timing model presented in Table 1. The averages of the residuals for each sidereal day are indicated in red. Right-hand plot: pre-fit residuals versus time obtained from the WSRT TOAs at 1380 MHz (black) and 345 MHz (red). The latter residuals are displayed with an offset of 60 μs for clarity. These were obtained using the timing model presented in Table 1. The lack of trends in the Westerbork residuals implies that our timing solution describes these TOAs correctly. These data were not used in the derivation of the timing solution presented in this paper; their inclusion does not change any parameter significantly.

may remain. On the other hand, there should be no correlation with orbital phase, hence orbital parameters should not be affected at all.

These excursions are likely to be caused by variations of the DM at time-scales of a few months that cannot be taken into account by the eight-polynomial model for the DM variations. The alternative explanations are not as plausible: an instability in the rotation of the pulsar would produce excursions with larger time-scales than those observed. The second derivative of the spin frequency [$\ddot{v} = (-0.6 \pm 2.3) \times 10^{-28} \text{ Hz s}^{-2}$] is consistent with zero, which suggests good long-term stability; the same is true for the third frequency derivative. Furthermore, the agreement between nearby daily residual averages suggests that the timing system used is stable.

To further verify the integrity of this timing solution, we compared its predictions with TOAs taken with the Westerbork Synthesis Radio Telescope (WSRT) in the Netherlands, which uses the Puma II coherent dedispersion back-end (Karuppusamy, Stappers & van Straten 2008). The 345 MHz data are especially useful because, in case of an inaccuracy in our DM model they would show significant trends. It is remarkable that despite the fact that the model represents mostly an interpolation during the 2009–2010 gap, no trends are discernible in either data set (see right-hand plot of Fig. 3).

2.4 Orbital model

The orbit of PSR J1738+0333 has a very low eccentricity, so we use the ‘ELL1’ orbital model (Lange et al. 2001) to model it.¹ This yields Keplerian and post-Keplerian parameters that are very weakly correlated with each other. Note that in order to estimate the ‘real’ eccentricity of the binary we assumed that the Shapiro delay is as predicted by GR for the values of M_c and $\sin i$ derived in Paper I. This assumption is safe because GR is known to provide a sufficiently accurate description of the distortion of space–time around weakly self-gravitating objects (Bertotti, Iess & Tortora 2003).

According to Freire & Wex (2010), the orthometric amplitude of the Shapiro delay (which quantifies the time amplitude of the *measurable* part of the Shapiro delay) is, for this system, given by $h_3 = 22 \text{ ns}$. Fitting for this quantity we obtain $h_3 = 9 \pm 13 \text{ ns}$. This is 1σ consistent with the prediction but the low relative precision of this measurement implies that we cannot determine M_c and $\sin i$ independently from the existing timing data. A precise measurement of the component masses of this system from Shapiro delay would require an improvement in timing precision that is much beyond our current capabilities.

In the right-hand plot of Fig. 4, we display the residuals as a function of the orbital phase. No trends are noticeable, either in the residuals or in their averages; this implies that the orbital model is not obviously flawed. This also suggests that the timing system is inherently stable. Furthermore, we see no DM variations as a function of the orbital phase (left-hand plot of Fig. 4), i.e. there are neither obvious spurious DM artefacts caused by incorrect folding nor detectable dispersive delays in the data.

¹ The ELL1 timing model as implemented in the TEMPO software package (<http://sourceforge.net/projects/tempo/>) is a modification of the DD timing model (Damour & Deruelle 1985, 1986) adapted to low-eccentricity binary pulsars. In terms of post-Keplerian observables, it contains all those which are numerically relevant for systems with $e \ll 1$. The ‘Einstein delay’ term is not relevant for such systems and is therefore not taken into account.

3 RESULTS

In what follows, we discuss some of the results of the timing programme. In Section 3.1 we briefly discuss the measurement of the parallax, which requires special care given the systematics highlighted in Section 2.3. Then in Section 3.2 we focus on the main result of the timing: the detection of the orbital decay of the system, \dot{P}_b . We compare it with the GR prediction in Section 3.3.

3.1 Parallax

As mentioned in Section 2.3, the quoted uncertainty for the parallax is likely to be too small given the systematic effects caused by uncorrected short-term DM variations. It is therefore important to gain a sense of whether this parallax estimate is accurate or if there are inconsistencies with other distance estimators.

The distance we obtain from this parallax ($d = 1.47 \pm 0.10 \text{ kpc}$) is consistent with the 1.4 kpc predicted by the NE2001 electron model of the Galaxy (Cordes & Lazio 2001) for the pulsar’s Galactic coordinates and DM. However, the distance estimates based on this model have been shown, in some cases, to significantly under- or overestimate real distances; therefore this agreement with the DM prediction cannot be used as solid evidence that our parallax is accurate.

This distance, when combined with the known temperature and photometric properties of the WD, produces an estimate for its radius that is very similar to that derived from its spectrum (see Paper I). This suggests that our value for the distance is likely to be accurate given the present timing uncertainties. This is important because the distance (and the proper motion, also presented in Table 1) is necessary for a correct estimate of the intrinsic orbital decay of the system \dot{P}_b^{Int} , as discussed below.

Following the analysis by Verbiest, Lorimer & McLaughlin (2010), we find that there are no significant biases affecting this parallax measurement.

3.2 Intrinsic orbital decay

The intrinsic orbital decay of the system can be obtained from the observed orbital period variation (\dot{P}_b) by subtracting the *kinematic effects* (Shklovskii 1970; Damour & Taylor 1991):

$$\dot{P}_b^{\text{Int}} = \dot{P}_b - \dot{P}_b^{\text{Acc}} - \dot{P}_b^{\text{Shk}}. \quad (1)$$

The same equation applies to any quantity with the dimension of time, like the spin parameters (P , \dot{P} and \dot{P}^{Int}).

The first term, $\dot{P}_b^{\text{Acc}} = a_T P_b/c$, is caused by the difference of accelerations of the PSR J1738+0333 system and the Solar system projected along the line of sight to the pulsar, a_T . This term is dominated by the difference of accelerations of the two systems caused by the average Galactic field, a_G : for the pulsar’s Galactic coordinates of $l = 27^\circ 7213$ and $b = 17^\circ 7422$ and distance, we obtain [using equation (5) in Nice & Taylor (1995), in combination with equation (17) in Lazaridis et al. 2009]

$$\frac{a_G}{c} P_b = 0.58_{-0.14}^{+0.16} \text{ fs s}^{-1}. \quad (2)$$

The a_T term also contains a contribution from nearby masses, a_S . Damour & Taylor (1991) present a statistical estimate of the magnitude of this effect for PSR B1913+16, which is dominated by large molecular clouds. For PSR J1738+0333, the same a_S would yield an orbital period derivative of

$$\left| \frac{a_S}{c} \right| P_b \lesssim 0.2 \text{ fs s}^{-1}, \quad (3)$$

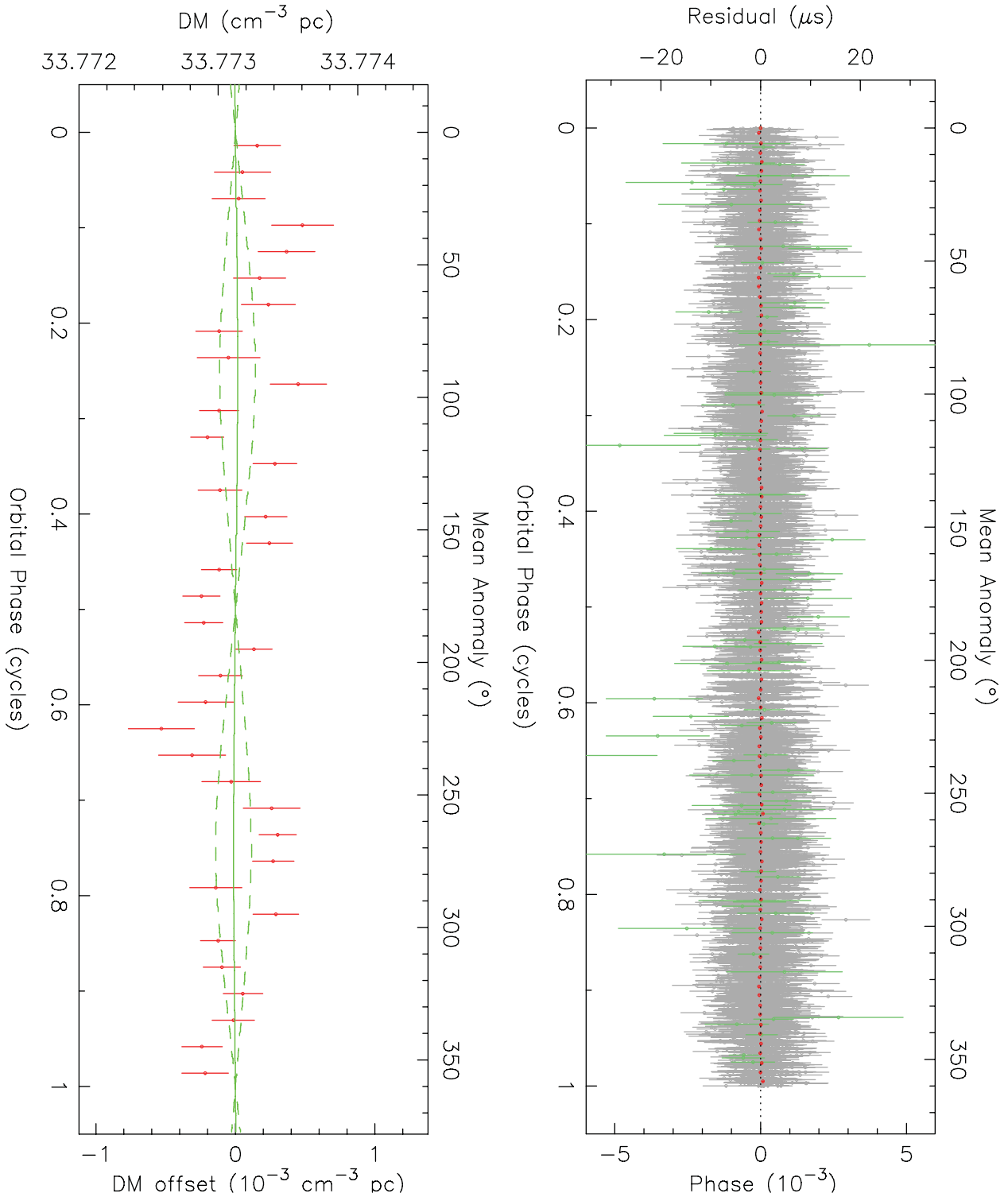


Figure 4. Left-hand plot: measured DM versus orbital phase. To the observed DMs we fit a DM variation model (green lines, see Appendix A) using DM and ΔDM as the free parameters, and display the resulting fits for the nominal and $\pm 2\sigma$ values of ΔDM . No significant variation as a function of orbital phase is detectable, indicating the lack of spurious artefacts in the data reduction and no outgassing from the companion. Right-hand plot: post-fit residuals versus orbital phase, which for this very low eccentricity system is measured from ascending node (i.e. the mean anomaly is equal to the orbital longitude). The residuals of the Parkes (green) and Arecibo (grey) TOAs were obtained with the timing model presented in Table 1. In red we indicate bin averages where the bin width is $0.01 P_b$. No significant trends can be identified in the residuals or their binned averages, indicating that the orbital model can describe the orbital modulation of the TOAs correctly. No dispersive delays or unaccounted Shapiro delay signatures are detectable near orbital phase 0.25, nor artefacts due to incorrect dedispersion and folding of the data.

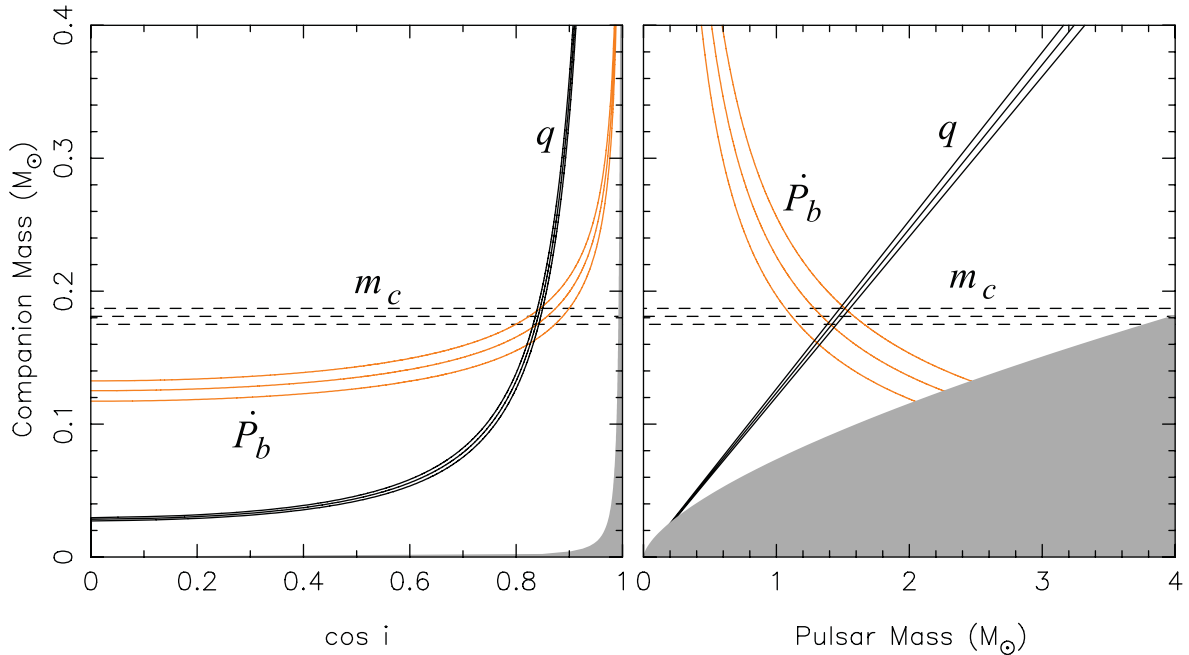


Figure 5. Constraints on system masses and orbital inclination from radio and optical measurements of PSR J1738+0333 and its WD companion. The mass ratio q and the companion mass m_c are theory-independent (indicated in black), but the constraints from the measured intrinsic orbital decay (\dot{P}_b^{Int} , in orange) are calculated assuming that GR is the correct theory of gravity. All curves intersect, meaning that GR passes this important test. Left-hand plot: $\cos i - m_c$ plane. The grey region is excluded by the condition $m_p > 0$. Right-hand plot: $m_p - m_c$ plane. The grey region is excluded by the condition $\sin i \leq 1$. Each triplet of curves corresponds to the most likely value and standard deviations of the respective parameters.

which is negligible. The a_S of PSR J1738+0333 is likely to be even smaller: although the pulsar is at a similar Galactocentric distance as PSR B1913+16, it is at a Galactic height of ~ 0.45 kpc, which is larger than that of PSR B1913+16: ~ 0.3 kpc.

The second kinematic effect in equation (1), commonly known as the ‘Shklovskii’ effect, caused by the centrifugal acceleration, is given by (Shklovskii 1970)

$$\dot{P}_b^{\text{Shk}} = (\mu_\alpha^2 + \mu_\delta^2) \frac{d}{c} P_b = 8.3^{+0.6}_{-0.5} \text{ fs s}^{-1}, \quad (4)$$

where μ_α and μ_δ are the proper motion in right ascension and declination (see Table 1). For the intrinsic \dot{P}_b , we thus obtain

$$\dot{P}_b^{\text{Int}} = -25.9 \pm 3.2 \text{ fs s}^{-1}. \quad (5)$$

3.3 Excess orbital decay

From the values for q and m_c in Paper I we can estimate the orbital decay caused by the emission of quadrupolar GWs for a low-eccentricity system, as predicted by GR:

$$\begin{aligned} \dot{P}_b^{\text{GR}} &\simeq -\frac{192\pi}{5} (n_b T_\odot m_c)^{5/3} \frac{q}{(q+1)^{1/3}} \\ &= -27.7^{+1.5}_{-1.9} \text{ fs s}^{-1}, \end{aligned} \quad (6)$$

where $n_b = 2\pi/P_b$ and $T_\odot \equiv GM_\odot c^{-3} = 4.925\,490\,947 \mu\text{s}$ (Lorimer & Kramer 2005). Subtracting this from \dot{P}_b^{Int} (equation 5) we obtain the ‘excess’ orbital decay relative to the prediction of GR,

$$\dot{P}_b^{\text{xs}} = 2.0^{+3.7}_{-3.6} \text{ fs s}^{-1}. \quad (7)$$

This is consistent with zero. As discussed in Section 4, this implies that GR passes the test posed by the orbital decay of PSR J1738+0333. We illustrate this match in Fig. 5, where we see that the

mass/inclination constraints, derived from \dot{P}_b^{Int} using equation (6) (i.e. assuming that GR is the correct theory of gravity), are consistent with the theory-independent² constraints derived from the optical observations.

3.4 Rigorous uncertainty estimates for orbital decay

To make reliable estimates of the uncertainties of these derived quantities (\dot{P}_b^{Gal} , \dot{P}_b^{Shk} , \dot{P}_b^{Int} and \dot{P}_b^{xs}), we implemented a new Monte Carlo routine in TEMPO2. From our list of 17476 TOAs, we created 220 000 similar data sets of fake TOAs that have random distributions consistent with the original TOAs and their uncertainties. For each fake TOA data set, we run TEMPO2 and record the resulting best-fitting parameters to disk. We then use the parallax of each simulation to estimate a_G and calculate the derived quantities for that simulation using the equations given above. Finally, in order to estimate \dot{P}_b^{xs} , we use a random (m_c, q) pair from the Monte Carlo simulation in Paper I, calculate the corresponding \dot{P}_b^{GR} and subtract this from \dot{P}_b^{Int} . This procedure is warranted by the intrinsic lack of correlation between the optical and radio measurements. The computer then calculates averages, standard deviations, medians and $\pm 1\sigma$ percentiles (presented in Table 1) for the resulting distributions of derived quantities. The averages and standard deviations are close to the estimated medians and 1σ percentiles, implying that the resulting distributions are generally close to Gaussian.

² By *theory-independent*, in the context of this paper, we denote quantities which are either based on weak-field gravity, which is known to be described extremely well by GR (Will 2006), or quantities which are free of any explicit strong-field deviations of gravity from GR, at least within the wide class of Lorentz-invariant gravity theories. The mass ratio in a binary pulsar system is an example of the latter (Damour 2009).

With this method, we are able to take into account any underlying correlations between the observables, thus estimating more reliable values and uncertainties for the derived quantities that depend only on the measured TOAs and their uncertainties.

4 GENERIC TESTS OF GRAVITY THEORIES

In order to understand the significance of the small value of \dot{P}_b^{xs} in equation (7) – the main experimental result of this paper – we now discuss what physical effects could in principle be contributing to it. According to Damour & Taylor (1991)

$$\dot{P}_b^{xs} = \dot{P}_b^M + \dot{P}_b^T + \dot{P}_b^D + \dot{P}_b^G, \quad (8)$$

where \dot{P}_b^M is due to mass loss from the binary, \dot{P}_b^T is a contribution from tidal effects, \dot{P}_b^D is the orbital decay caused mainly by the emission of dipolar GWs (and any extra multipole modifying the general relativistic prediction) and \dot{P}_b^G is a contribution from possible (yet undetected) variations of Newton's gravitational constant (as measured by a Cavendish experiment). The first two terms are the ‘classical’ terms, and the last two would only be non-zero for theories of gravity other than GR.

4.1 Classical terms

4.1.1 Mass loss

In Appendix A, we derive an upper limit for the mass loss from the companion as a function of the total mass of the system. For the pulsar, the mass loss is dominated by the loss of rotational energy (Damour & Taylor 1991):

$$\frac{\dot{M}_p}{M_t} = \frac{\dot{E}}{M_t c^2} = 1.5 \times 10^{-21} \text{ s}^{-1}, \quad (9)$$

which is of the same order as the upper limit for $\frac{\dot{M}_c}{M_t}$.

The contribution to the orbital variation due to the total mass loss $\dot{M} = \dot{M}_c + \dot{M}_p$ is given by (Damour & Taylor 1991)

$$\dot{P}_b^M = 2 \frac{\dot{M}}{M_t} P_b < 0.2 \text{ fs s}^{-1}, \quad (10)$$

which is about 20 times smaller than the current uncertainty in the measurement of \dot{P}_b^{xs} .

4.1.2 Tidal orbital decay

We now calculate the orbital decay caused by tides. From equations (3.15) and (3.19) in Smarr & Blandford (1976), we derive the following expression for \dot{P}_b^T :

$$\dot{P}_b^T = \frac{k\Omega_c}{3\pi q(q+1)} \left(\frac{R_c P_b \sin i}{xc} \right)^2 \frac{1}{\tau_s}. \quad (11)$$

Unlike the expressions in equation (3.19), this equation is exact because it relates the synchronization time-scale τ_s (which describes the change in the companion angular velocity Ω_c , $\tau_s = -\Omega_c/\dot{\Omega}_c$) to the time-scale associated with the change in the orbital period ($\tau_p = P_b/\dot{P}_b^T$) assuming only conservation of the angular momentum. In this expression $k \equiv I_c/(M_c R_c^2)$, where I_c is the WD moment of inertia. WDs (particularly those with a mass much below the Chandrasekhar limit) are sustained by the degeneracy pressure of non-relativistic electrons and can be well approximated by a polytropic sphere with $n = 1.5$. For such stars, we have $k = 0.2$ (Motz 1952).

The only unknown parameters in this expression are Ω_c and τ_s . If τ_s is much smaller than the characteristic age of the pulsar $\tau_c = 4.1$ Gyr, then the WD rotation is already synchronized with the orbit ($\Omega_c = n_b$) and there are no tidal effects at all. If, on the other hand, $\tau_s > \tau_c$, then Ω_c can be much larger, but it must still be smaller than the break-up angular velocity $\Omega_c < \sqrt{GM_c/R_c^3} = 0.038 \text{ rad s}^{-1}$. These conditions for Ω_c and τ_s yield $\dot{P}_b^T < 1.4 \text{ fs s}^{-1}$. Thus, even if the WD were rotating near break-up velocity, \dot{P}_b^T would still be smaller than the uncertainty in the measurement of \dot{P}_b^{xs} . We note, however, that the progenitor of the WD was very likely synchronized with the orbit. This implies that, when the WD formed, its rotational frequency was within one order of magnitude of the orbital frequency, i.e. $\Omega_c \lesssim 2 \times 10^{-3} \text{ rad s}^{-1}$ (for the reasoning, see e.g. appendix B2.2 of Bassa et al. 2006).

4.2 Test of GR and generic tests of alternative gravity theories

The smallness of the classical terms implies that the measurement of \dot{P}_b^{xs} (equation 7) is a direct test of GR. Unlike many alternative theories of gravity, GR predicts $\dot{P}_b^G = 0$, $\dot{P}_b^D = 0$ and therefore $\dot{P}_b^{xs} = 0$. As discussed in Section 3.3, this is consistent with observations, which means that GR passes the test posed by the measurement of \dot{P}_b^{xs} for PSR J1738+0333. In this respect PSR J1738+0333 constitutes a verification of GR's quadrupole formula with a precision of about 15 per cent at the 1σ level. In view of more stringent tests with other binary pulsars (Kramer et al. 2006; Weisberg, Nice & Taylor 2010) this result by itself does not seem particularly interesting. However, the large difference in the compactness of the two components of this binary system makes PSR J1738+0333 a remarkable laboratory for alternative gravity theories, in particular those which predict the emission of dipolar gravitational radiation. In Sections 5 and 6, we will confront our observations with two specific classes of gravity theories. In the present section, we follow a more generic approach, valid for gravity theories where non-perturbative strong-field effects are absent and higher-order contributions in powers of the gravitational binding energies of the bodies can be neglected, at least to a point where one does not care about multiplicative factors $\lesssim 2$. As an example, the well-known Jordan–Fierz–Brans–Dicke scalar–tensor theory falls into this group.

Under the assumptions given above, the change in the orbital period caused by dipolar gravitational radiation damping in a low-eccentricity binary pulsar system is given by

$$\dot{P}_b^D \simeq -2\pi n_b T_\odot m_c \frac{q}{q+1} \kappa_D S^2 + \mathcal{O}(s_{p,c}^3), \quad (12)$$

where $S = s_p - s_c$ is the body-dependent term which is given by the difference in the ‘sensitivities’ of the pulsar, s_p , and the companion, s_c (see Will 1993 for the definition of $s_{p,c}$). The quantity κ_D is a body-independent constant that quantifies the dipolar self-gravity contribution, and takes different values for different theories of gravity.³ For the purpose of this section, we have neglected higher-order corrections in powers of the sensitivities in the above-given equation (They actually vanish in the Jordan–Fierz–Brans–Dicke case.). The full non-linearity will be taken into account in Sections 5 and 6 (anticipating on the notation defined there, the terms $\propto s_{p,c}^3$ are negligible when the absolute value of the non-linear matter–scalar coupling constant, $|\beta_0|$, is significantly smaller than 2).

³ In general scalar–tensor theories of gravity, we have $\kappa_D = 2\eta^2(1 - \gamma^{PPN})^{-1}$, where $\eta \equiv 4\beta^{PPN} - \gamma^{PPN} - 3$ is the Nordtvedt parameter, a combination of post-Newtonian parameters (PPN) related to the violation of the strong equivalence principle.

The value of $s_{p,c}$ depends on the theory of gravity, the exact form of the equation of state (EOS) and the mass of the pulsar; for a $M_p = 1.4 M_\odot$ neutron star, it is generally of the order of 0.15, the value we use in our calculations. For an asymmetric system like PSR J1738+0333, the sensitivity of the companion WD has a negligible value: in the post-Newtonian limit, it is given by $\epsilon/M_c c^2 \sim 10^{-4}$, where ϵ is the gravitational binding energy of the WD (Will 2006). Therefore, $\mathcal{S} = s_p - s_c \simeq s_p \neq 0$, which implies that if $\kappa_D \neq 0$, then there must be emission of dipolar GWs, and an associated orbital decay according to equation (12). In a double neutron star system we would have $s_p \approx s_c$ and therefore $\mathcal{S} \approx 0$, which means that we should observe $\dot{P}_b^D \approx 0$ even if $\kappa_D \neq 0$. It is for this reason that, despite the low relative precision of the radiative test in PSR J1738+0333, it represents such a powerful constraint on alternative theories of gravity (see e.g. Eardley 1975; Bhat, Bailes & Verbiest 2008). Apart from this, the use of optical data is very important because they provide estimates of q and m_c that are free of explicit strong-field effects – unlike in the case of the binary pulsar PSR B1913+16 (see Weisberg et al. 2010), or for many of the parameters of the double pulsar (Kramer et al. 2006).

The last contribution to \dot{P}_b^{xs} comes from a possible contribution to the orbital change by a varying gravitational constant (\dot{P}_b^G in equation 8). In the worst case, \dot{P}_b^D and \dot{P}_b^G could both be large (in violation of GR) but just happen to cancel each other in the PSR J1738+0333 system because of different signs. To disentangle these effects there are two methods. First, one can use the best current limits from tests in the Solar system, notably Lunar Laser Ranging (LLR), which yields $\dot{G}/G = (-0.7 \pm 3.8) \times 10^{-13} \text{ yr}^{-1}$ (Hofmann, Müller & Biskupek 2010), and obtain for PSR J1738+0333 an (conservative) upper limit of

$$\dot{P}_b^G = -2 \frac{\dot{G}}{G} P_b = (+0.14 \pm 0.74) \text{ fs s}^{-1} \quad (13)$$

(Damour, Gibbons & Taylor 1988; Damour & Taylor 1991). Therefore, $\dot{P}_b^D = \dot{P}_b^{xs} - \dot{P}_b^G = 1.9_{-3.7}^{+3.8} \text{ fs s}^{-1}$, which yields, for a typical sensitivity $s_p = 0.15$

$$\kappa_D = (-0.8 \pm 1.6) \times 10^{-4}, \quad (14)$$

a limit that is a factor of 8 more stringent than the limit from PSR J1012+5307 (Lazaridis et al. 2009).

The second method, developed in Lazaridis et al. (2009), combines two binary pulsar systems with different orbital periods. The method is based on the fact that a wide orbit is more sensitive to a change in the gravitational constant but less affected by the emission of dipolar GWs, in comparison to a more compact orbit. If we combine the \dot{P}_b^{xs} of PSR J1738+0333 with that of a binary pulsar with a longer orbital period we obtain a simultaneous test for κ_D and \dot{G} .

When calculating \dot{P}_b^G for a combined limit on κ_D and \dot{G} based on two binary pulsars, we need to account for mass variations in compact stars as a result of a changing gravitational constant. Otherwise our limit on \dot{G} will be too tight (Nordtvedt 1990). As a first approximation, that only accounts for the influence of the local value of G , we can use equation (18) in Nordtvedt (1990):

$$\dot{P}_b^G = -2 \frac{\dot{G}}{G} \left(1 - \frac{2q+3}{2q+2} s_p - \frac{3q+2}{2q+2} s_c \right) P_b. \quad (15)$$

As in equation (12), the contribution from the sensitivity of the WD companion, s_c , can be neglected. For PSR J1738+0333, the correction factor due to the sensitivities (i.e. the parenthesis on the right-hand side of equation 15) is about 0.85.

As in Lazaridis et al. (2009), we use the \dot{P}_b^{xs} of PSR J0437–4715 (Deller et al. 2008; Verbiest et al. 2008) to complement our \dot{P}_b^{xs}

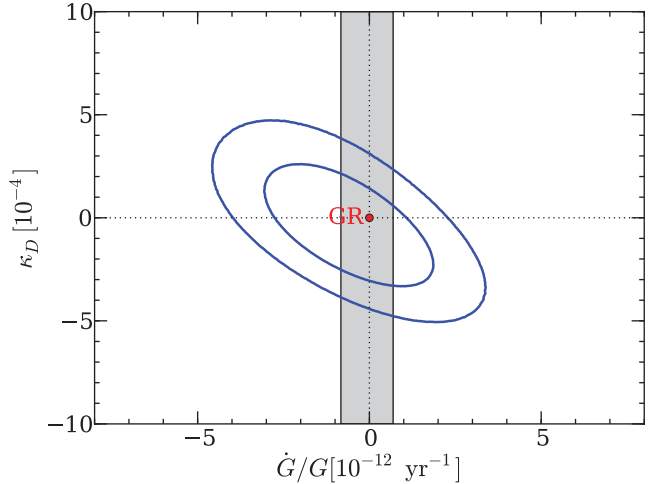


Figure 6. Limits on \dot{G}/G and κ_D derived from the measurements of \dot{P}_b^{xs} of PSR J1738+0333 and PSR J0437–4715. The inner blue contour level includes 68.3 per cent and the outer contour level 95.4 per cent of all probability. At the origin of coordinates, GR is well within the inner contour and close to the peak of probability density. The grey band includes regions consistent with the measured value and 1σ uncertainty of \dot{G}/G from LLR. Generally only the upper half of the diagram has physical meaning, as the radiation of dipolar GWs must necessarily make the system lose orbital energy.

measurement (see equation 7). PSR J0437–4715 has a slightly higher mass than PSR J1738+0333, and we will account for this in the sensitivity by having s_p scale proportional to the mass, as suggested by equation (B.3) of Damour & Esposito-Farèse (1992). The joint probability density function for \dot{G}/G and κ_D is displayed in Fig. 6. At the origin of coordinates, GR is well within the inner 68 per cent contour and close to the peak of probability density, i.e. it is consistent with the experimental results from these two binaries. Marginalizing this probability distribution function, we obtain

$$\begin{aligned} \dot{G}/G &= (-0.6 \pm 1.6) \times 10^{-12} \text{ yr}^{-1} \\ &= (-0.009 \pm 0.022) H_0, \end{aligned} \quad (16)$$

$$\kappa_D = (-0.3 \pm 2.0) \times 10^{-4}, \quad (17)$$

where H_0 is Hubble's constant (Riess et al. 2009) and the uncertainties are 1σ . The \dot{P}_b^{xs} measurement of PSR J0437–4715 is mostly responsible for the limit on \dot{G}/G , and it has therefore not improved since Lazaridis et al. (2009). The \dot{P}_b^{xs} measurement of PSR J1738+0333 is mostly responsible for the limit on κ_D , which has improved by a factor of ~ 6 since Lazaridis et al. (2009). Although the limit on \dot{G}/G derived from binary pulsar experiments is one order of magnitude less restrictive than that derived from LLR, it is of interest because it represents an independent test.

The analysis presented in this section is restricted to gravity theories that do not develop non-perturbative strong-field effects in neutron stars. This assumption is well justified for PSR J1738+0333, since such effects do not seem to exist in other binary pulsars with similar masses, or even with a higher mass like in the case of PSR J1012+5307 (Lazaridis et al. 2009). Even when non-perturbative effects do develop, we will show below that the higher-order corrections entering equation (12) do not change the conclusions qualitatively.

5 CONSTRAINTS ON SCALAR-TENSOR THEORIES OF GRAVITY

The most natural alternatives to GR involve a scalar field φ contributing to the gravitational interaction, in addition to the metric $g_{\mu\nu}$ describing usual spin-2 gravitons. In these theories, matter is assumed to be universally coupled to a physical metric $\tilde{g}_{\mu\nu} \equiv A^2(\varphi)g_{\mu\nu}$, where $A(\varphi)$ is a non-vanishing function defining the matter–scalar coupling.

It is convenient to expand this function around the background value φ_0 imposed by the cosmological evolution, as $\ln A(\varphi) = \ln A(\varphi_0) + \alpha_0(\varphi - \varphi_0) + \frac{1}{2}\beta_0(\varphi - \varphi_0)^2 + \dots$, where α_0 defines the linear matter–scalar coupling constant, β_0 the quadratic coupling of matter to two scalar particles, and we will not consider higher-order vertices in the following (those corresponding to α_0 and β_0 are diagrammatically represented on the axes of Figs 7 and 8, the circles meaning a matter source). GR corresponds to $\alpha_0 = \beta_0 = 0$, and the Brans–Dicke theory (Jordan 1959; Fierz 1956; Brans & Dicke 1961) to $\alpha_0^2 = 1/(2\omega_{BD} + 3)$ and $\beta_0 = 0$.

The predictions of such theories have been carefully studied in the literature (Will 1993; Damour & Esposito-Farèse 1992, 1993, 1996a,b, 1998). In strong-field conditions, notably within and near a neutron star, the coupling constants α_0 and β_0 are modified by self-gravity effects, and become body-dependent quantities, α_A and β_A (A being a label for the body), which can be computed by numerical integration of the field equations. One needs to assume a specific EOS for nuclear matter in such integrations, and we will use the moderate one of Damour & Esposito-Farèse (1996b) in the

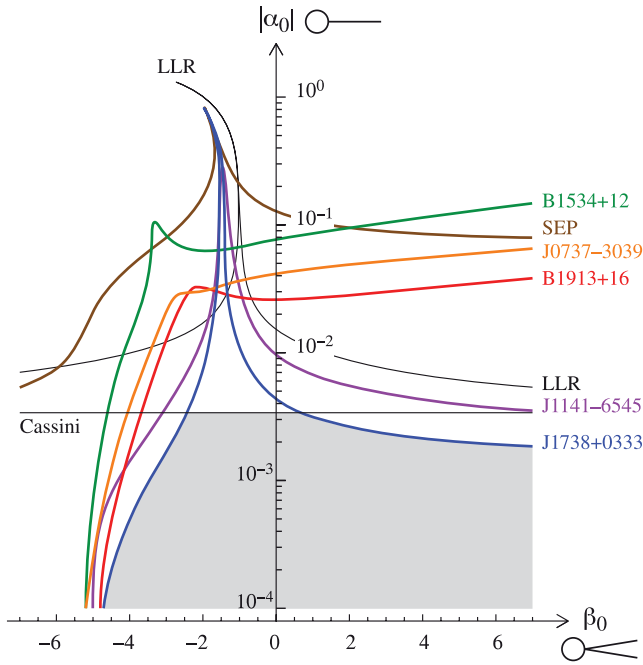


Figure 7. Solar system and binary pulsar 1σ constraints on the matter–scalar coupling constants α_0 and β_0 . Note that a logarithmic scale is used for the vertical axis $|\alpha_0|$, i.e. that GR ($\alpha_0 = \beta_0 = 0$) is sent at an infinite distance down this axis. LLR stands for Lunar Laser Ranging, Cassini for the measurement of a Shapiro time-delay variation in the Solar system, and SEP for tests of the strong equivalence principle using a set of neutron star–WD low-eccentricity binaries (see text). The allowed region is shaded, and it includes GR. PSR J1738+0333 is the most constraining binary pulsar, although the Cassini bound is still better for a finite range of quadratic coupling β_0 .

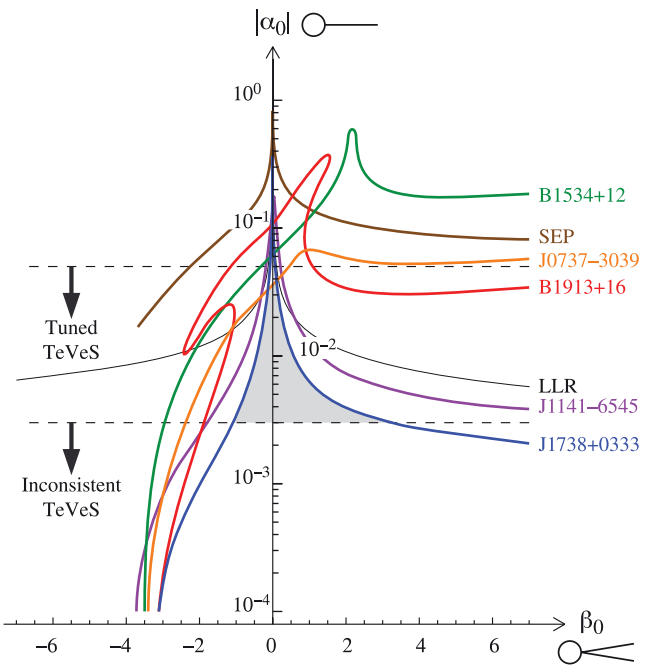


Figure 8. Similar theory plane as in Fig. 7, but now for the (non-conformal) matter–scalar coupling described in the text, generalizing the TeVeS model. Above the upper horizontal dashed line, the non-linear kinetic term of the scalar field may be a natural function; between the two dashed lines, this function needs to be tuned; and below the lower dashed line, it cannot exist any longer. The allowed region is shaded. It excludes GR ($\alpha_0 = \beta_0 = 0$) because such models are built to predict MOND at large distances. Note that binary pulsars are more constraining than Solar system tests for this class of models (and that the Cassini bound of Fig. 7 does not exist any longer here). For a generic non-zero β_0 , PSR J1738+0333 is again the most constraining binary pulsar, while for $\beta_0 \approx 0$, the magnitude of $|\alpha_0|$ is bounded by the J0737–3039 system.

following. The dependence on the stiffness of the EOS is illustrated in Damour & Esposito-Farèse (1998), but this does not change the relative strength of the various binary–pulsar tests.

The body-dependent parameters α_A and β_A enter all observable predictions, and for instance, the effective gravitational constant between two bodies A and B reads

$$\tilde{G}_{AB} \equiv G_* A^2(\varphi_0) \cdot (1 + \alpha_A \alpha_B), \quad (18)$$

where G_* denotes Newton’s bare constant.⁴ This induces a generic time dependence of the gravitational constant (cf. equation 15), as well as a violation of the strong equivalence principle (SEP): the acceleration of a body depends on its gravitational binding energy. Let us also quote the expressions taken by the generalizations of Eddington’s PPN parameters γ^{PPN} and β^{PPN} (Eddington 1923), as the former will differ in Section 6:

$$\gamma_{AB} \equiv 1 - 2 \frac{\alpha_A \alpha_B}{1 + \alpha_A \alpha_B}, \quad (19)$$

$$\beta_{BC}^A \equiv 1 + \frac{1}{2} \frac{\beta_A \alpha_B \alpha_C}{(1 + \alpha_A \alpha_B)(1 + \alpha_A \alpha_C)}, \quad (20)$$

where A, B, C denote a priori three bodies, but $B = C$ is allowed. The relativistic periastron advance, proportional to $(2 + 2\gamma^{PPN} - \beta^{PPN})$

⁴ Newton’s constant G , as measured in the Cavendish experiment, is given by $G_* A^2(\varphi_0)(1 + \alpha_0^2)$.

in the PPN formalism, becomes now a combination of the above given expressions, explicitly written in equation (9.20a) of Damour & Esposito-Farèse (1992).

But the most spectacular deviation from GR is that scalar waves are now also emitted by any binary system, thus contributing to the observed variation of the orbital period. For asymmetric systems, notably the neutron star–WD binary studied in the present paper, the main contribution comes from dipolar waves:

$$\dot{P}_b^D = -2\pi n_b \frac{G_* M_c}{c^3} \frac{q}{q+1} \frac{1+e^2/2}{(1-e^2)^{5/2}} (\alpha_p - \alpha_c)^2, \quad (21)$$

where the eccentricity e is negligible in our case. [The lowest-order expansion of $(\alpha_p - \alpha_c)^2$ in powers of the sensitivities $s_{p,c}$ is denoted as $\kappa_D S^2$ in equation (12). In the present section, we are numerically taking into account the full non-linear dependence on the bodies' self-gravity.] The companion's scalar charge $\alpha_c \approx \alpha_0$ because of its small binding energy, while the pulsar's scalar charge α_p may be of the order of 1 in some theories even if $\alpha_0 \approx 0$ (Damour & Esposito-Farèse 1993, 1996b). The orbital decay from dipolar GW emission (equation 21), which is of order $\mathcal{O}(1/c^3)$, is thus generically much larger than the usual quadrupole of order $\mathcal{O}(1/c^5)$. An observed \dot{P}_b consistent with GR therefore strongly constrains scalar-tensor theories.

This is illustrated in Fig. 7, where we also display the 1σ constraints imposed by Solar system tests (the Cassini measurement of the Shapiro delay, see Bertotti et al. 2003, and the aforementioned LLR experiment, Hofmann et al. 2010) and binary pulsars, according to the latest literature (see Weisberg et al. 2010, for PSR B1913+16, Stairs et al. 2002 for PSR B1534+12, Kramer et al. 2006 for PSR J0737–3039A/B, Bhat et al. 2008 for PSR J1141–6545 and Gonzalez et al. 2011 for the SEP test with an ensemble of binary pulsars with wide orbits and low eccentricities). For PSRs B1913+16 and B1534+12, we multiplied the error bars on their measured \dot{P}_b^{Int} by two because of the known uncertainties on their distances, which preclude an accurate estimate of the kinematic contributions to their orbital decay.

Note that the LLR constraints present a (deformed) vertical asymptote at $\beta_0 = -1$, whereas SEP and dipolar-radiation-dominated constraints (from PSRs J1738+0333 and J1141–6545) exhibit one for $\beta_0 \approx -1.5$. This difference comes from the higher-order corrections in powers of the sensitivities that we neglected in equation (12) but which are taken into account in the present section. These higher-order terms are vanishingly small in the Earth–Moon system relevant to LLR, but they are numerically significant for neutron stars, and can even dominate the lowest-order contributions. This is notably the case when $\beta_0 = -1 - \alpha_0^2$, which implies $\kappa_D = 0$ and a dipolar radiation actually starting at order $\mathcal{O}(s^4)$ instead of $\mathcal{O}(s^2)$. However, the proximity of these two vertical asymptotes illustrates that Fig. 7 would keep a similar shape even if we neglected all higher-order corrections. This would just slightly shift the various curves, as would a different choice of the nuclear EOS. This justifies a posteriori the lowest-order truncation used in our analysis in Section 4.2, even for non-negligible values of $|\beta_0|$. For large values of this coupling constant, the higher-order terms are responsible for the dissymmetry of Fig. 7 with respect to the sign of $1 + \beta_0$.

A comment on the companion mass used in equation (21). The mass of the WD companion is derived from the optical data of Paper I, which yields GM_c , and not G_*M_c . The difference is a negligible factor $1 + \alpha_0^2$, which we anyway take into account when calculating the constraints on the matter–scalar coupling constants α_0 and β_0 .

Fig. 7 shows that scalar–tensor theories with a quadratic matter–scalar coupling $\beta_0 < -5$ are forbidden, whatever the value of the linear coupling α_0 . This is due to the non-perturbative strong-field effects studied in Damour & Esposito-Farèse (1993, 1996b). For $\beta_0 > -5$, the limits on α_0 are now derived either from the Cassini experiment or from PSR J1738+0333. For positive β_0 , Solar system tests used to provide the best constraints on α_0 , but this has recently changed: PSR J1141–6545 (Bhat et al. 2008) is more constraining than the Solar system tests for $\beta_0 \gtrsim 7$ and PSR J1738+0333 is now the most constraining of all for $\beta_0 > 0.7$. The same is true for the $-4.8 < \beta_0 < -2.4$ range. The special case $\beta_0 = 0$ (the Jordan–Fierz–Brans–Dicke theory of gravity) is in the region where the Cassini experiment is still more sensitive. Our 1σ pulsar limit $\alpha_0^2 < 2 \times 10^{-5}$ converts into $\omega_{\text{BD}} > 25\,000$. This is within a factor of 1.7 of the precision of the Cassini experiment. We obtain the same constraint in the massive Brans–Dicke theories recently considered in Alsing et al. (2011) when the scalar's mass $m_s c^2 < h/P_b = 1.35 \times 10^{-19}$ eV (where h is Planck's constant), and no longer any significant constraint for larger scalar masses, consistently with Fig. 1 of that reference.

Overall, PSR J1738+0333 provides significantly better constraints than the previous best binary pulsar experiment, PSR J1141–6545 (Fig. 7). If the limits obtained with that or other systems improve in the near future that would represent an important confirmation of the results obtained in this paper.

6 CONSTRAINTS ON TEVES-LIKE THEORIES

A tensor–vector–scalar theory of gravity has been proposed by Bekenstein (2004) to account for galaxy rotation curves and weak lensing without the need for dark matter. This is a relativistic realization of the MOND proposal (Milgrom 1983), which introduces a fundamental acceleration scale $a_0 \approx 10^{-10} \text{ m s}^{-2}$ (not to be confused with the matter–scalar coupling constant α_0 defined above). One of the difficulties is to be able to predict significant deviations from Newtonian gravity at large distances, while being consistent with Solar system and binary–pulsar tests of GR at smaller scales (Sanders 1997; Bruneton & Esposito-Farèse 2007). Indeed, the scalar-field kinetic term of TeVeS is an unknown non-linear function, which must take different forms at small and large distances. This function can have a natural shape only if $|\alpha_0| > \sqrt{r_{\odot U}/r_{\text{MOND}}} \approx 0.05$, where $r_{\odot U}$ is the orbital radius of Uranus and $r_{\text{MOND}} = \sqrt{GM_{\odot}/a_0} \approx 7000 \text{ au} \approx 0.1 \text{ lt-yr}$, otherwise the model would predict anomalies too large to be consistent with planetary ephemerides (Laskar et al. 2009). Below this value, the function needs to be tuned, and even fine-tuned for much smaller $|\alpha_0|$, and it merely cannot exist any longer if $|\alpha_0| < r_{\odot U}/r_{\text{MOND}} \approx 0.003$ (it would need to be bi-valued). Using binary pulsars to constrain the matter–scalar coupling constant α_0 within TeVeS is thus particularly interesting.

In the following, we shall not take into account all the subtle details of TeVeS, which are not relevant for our conclusions. In particular, Bekenstein introduced specific scalar–vector couplings to avoid superluminal propagation, but this is actually not necessary to respect causality (Bruneton 2007; Bruneton & Esposito-Farèse 2007; Babichev, Mukhanov & Vikman 2008). We will thus focus on the small-distance behaviour of this theory, and assume that the scalar-field kinetic term takes its standard form in this limit. We will also neglect the contributions of the vector field to the dynamics and the gravitational radiation, because they depend again on some coupling constant which can be chosen small enough. Let us just underline that if the vector field carries away some significant

amount of energy, then binary–pulsar data are even more constraining than what we obtain below. Neglecting these contributions is thus a conservative choice. To simplify, we will here assume that the vector field of TeVeS is aligned with the proper time direction of matter.

The crucial difference of TeVeS, with respect to the standard scalar–tensor theories of Section 5, is the expression of the physical metric $\tilde{g}_{\mu\nu}$ to which matter is universally coupled. In the rest frame of matter, it reads $\tilde{g}_{00} = A^2(\varphi)g_{00}$ for the time component, but $\tilde{g}_{ij} = A^{-2}(\varphi)g_{ij}$ for the spatial ones. The actual model constructed in Bekenstein (2004) assumes $A(\varphi) = \exp(\alpha_0\varphi)$, but we shall here generalize it and write $\ln A(\varphi) = \ln A(\varphi_0) + \alpha_0(\varphi - \varphi_0) + \frac{1}{2}\beta_0(\varphi - \varphi_0)^2$, as in Section 5. We are thus considering here a class of TeVeS-like theories rather than the single model of Bekenstein (2004).

This specific form of the physical metric results in several important differences with respect to Section 5. First of all, to compute the matter–scalar coupling parameters α_A and β_A corresponding to a strongly self-gravitating body A , one must numerically integrate new field equations. To save space, we just quote here the differences with respect to Damour & Esposito-Farèse (1996b), where the standard scalar–tensor case was discussed in detail: all factors $A^4(\varphi)$ in its equations (3.6a,b,d,e,h) and (3.14d,h) should be replaced by $A^{-2}(\varphi)$, while the factor $A^3(\varphi)$ of its equation (3.6f) should become $A^{-3}(\varphi)$. Finally, the $(\tilde{\varepsilon} - 3\tilde{p})$ term of its equations (3.6d) and (3.14d) should be replaced by the sum $(\tilde{\varepsilon} + 3\tilde{p})$. [On the other hand, note that the $(\tilde{\varepsilon} - \tilde{p})$ term of its equation (3.6d) does not change, nor does the sign of $\alpha(\varphi)$ in its equation (3.6e).] These modifications are consistent with the results of Lasky, Sotani & Giannios (2008). After numerically integrating these field equations, starting from central values of the scalar field and matter density, one can extract the mass of the neutron star and its effective scalar charge α_A in the same way as in Damour & Esposito-Farèse (1996b). The effective quadratic coupling β_A is then defined as $\partial\alpha_A/\partial\varphi_0$ for a fixed baryonic mass. For some binary–pulsar tests, it is also necessary to compute the star’s moment of inertia, and its derivative with respect to the background scalar field φ_0 at constant baryonic mass.

The form of the physical metric also changes the post-Newtonian predictions of the theory. Instead of equations (18) and (19), we now get

$$\tilde{G}_{AB} = G_*(1 + \alpha_A\alpha_B), \quad (22)$$

$$\gamma_{AB} = \gamma^{\text{PPN}} = 1, \quad (23)$$

while equation (20) is unchanged. Note that the effective gravitational constant \tilde{G}_{AB} does not depend any longer on $A^2(\varphi_0)$. In the actual TeVeS theory of Bekenstein (2004), where $\beta_0 = 0$, the weak-field effective gravitational constant is thus a true constant given by $G_*(1 + \alpha_0^2)$, in particular time-independent as was first derived in Bekenstein & Sagi (2008). This constancy also explains why LLR and other SEP tests do not constrain at all the theories with $\beta_0 = 0$, as illustrated in Fig. 8.

The expression for the periastron advance takes the same form as in standard scalar–tensor theories in terms of γ_{AB} and β_{BC}^A , but now with $\gamma_{AB} = 1$. In the weak-field conditions of the Solar system, the fact that $\gamma^{\text{PPN}} = 1$, like in GR, explains why the Cassini time-delay experiment does not provide any constraint on TeVeS-like theories.

All the other predictions of scalar–tensor theories, including the dipolar damping given by equation (21), keep the same forms in terms of the body-dependent quantities α_A and β_A , but their numerical values do differ because of the numerical integrations described above. For $\beta_0 = 0$, i.e. the actual TeVeS theory of Bekenstein (2004), one finds that $\alpha_A = \alpha_0$ independently of the body. This can be de-

duced from equation (4.14) of Damour & Esposito-Farèse (1996a), where the scalar field is no longer sourced by the trace of the energy-momentum tensor, as in standard scalar–tensor theories, but by the same combination $(\tilde{\varepsilon} + 3\tilde{p})$ as the gravitational potential. The constancy of $\alpha_A = \alpha_0$, when $\beta_0 = 0$, is also confirmed by our numerical integrations. The consequence of this extra symmetry of TeVeS is that the dipolar radiation predicted by equation (21) merely vanishes, and asymmetrical neutron star–WD binaries like PSR J1738+0333 no longer provide any stringent constraints. This is illustrated in Fig. 8, where several binary–pulsar tests now present a bump on the vertical axis, $\beta_0 = 0$. As compared to Fig. 7, the main effect of the non-conformal matter–scalar coupling assumed in TeVeS-like models is thus to displace these bumps from $\beta_0 \sim -1$ or -2 to the axis $\beta_0 = 0$.

For generic TeVeS-like models with $|\beta_0| > 0.1$, we find again that PSR J1738+0333 is the most constraining binary pulsar. We also note that several binary pulsar tests are now *more* constraining than all Solar system experiments [i.e. the LLR line of Fig. 8, while the perihelion shift of Mercury (Shapiro 1990) gives even weaker constraints, and all deflection or time-delay predictions coincide with those of GR at the first post-Newtonian order].

From a theoretical point of view, the most natural value of the linear matter–scalar coupling constant $|\alpha_0|$ would be of the order of unity. Fig. 8 shows this is experimentally forbidden, even on the vertical axis $\beta_0 = 0$, thanks to several binary pulsars whose tests do not rely on the magnitude of the dipolar radiation.⁵ They actually impose that $|\alpha_0| < 0.035 < \sqrt{r_{\odot U}/r_{\text{MOND}}}$, therefore TeVeS needs to assume an unnatural shape of the function defining its scalar’s dynamics.

A possible way to avoid fine-tuning in TeVeS-like models has been proposed in Babichev, Deffayet & Esposito-Farèse (2011), where it was shown that $|\alpha_0| = 1$ can be consistent with Solar system and binary–pulsar tests, thanks to a screening of all scalar-field effects at small distances. Therefore, the results of the present paper do not rule out TeVeS, but show that its original 2004 formulation by Bekenstein may need to be amended. At present, even its original writing is consistent, although it does need some tuning.

7 CONCLUSIONS AND PROSPECTS

It is quite fortunate that the timing precision of PSR J1738+0333 allows a precise measurement of the key observables necessary for an estimation of the intrinsic orbital decay (\dot{P}_b , μ_α , μ_δ and π_x) and that the optical observations provide a precise estimate of a general relativistic prediction for the orbital decay, thus allowing a stringent limit on the emission rate for dipolar GWs. As a result of this, PSR J1738+0333 is already the most constraining binary pulsar for (conformally coupled) scalar–tensor theories of gravity.

PSR J1738+0333 is also the most constraining test of TeVeS-like theories when the quadratic matter–scalar coupling constant $|\beta_0| \gtrsim 0.1$. In fact, for $\beta_0 < -1$ and $\beta_0 > 3$, such theories are excluded altogether. Bekenstein’s TeVeS (a special case with $\beta_0 = 0$) is still allowed by the results of this experiment, but already needs some tuning given the small limit $|\alpha_0| < 0.035$ that we obtain from the double pulsar results (Kramer et al. 2006). We note that the precision of the latter result has greatly improved since 2006 and will be presented in a forthcoming publication (Kramer et al.,

⁵ The two ‘horns’ of the constraints imposed by PSR B1913+16 come from the fact that this system provides only three post-Keplerian observables, i.e. only one test, and some fine-tuned models can thus pass it.

in preparation). This will significantly reduce the allowed values of $|\alpha_0|$ in the gap around $\beta_0 = 0$. As a consequence, all surviving TeVeS-like theories will have to be unnaturally fine-tuned, including Bekenstein's TeVeS.

Continued timing of PSR J1738+0333 will give us a much more precise measurement of \dot{P}_b and (to a smaller extent) of π_x . This will allow a further improvement of the estimate of the intrinsic orbital decay. However, unless we can make a more precise determination of m_c , we will not be able to improve upon the current estimate of \dot{P}_b^{GR} ; this implies that the precision of this test is unlikely to improve by more than a factor of 2. Despite that, a precise measurement of \dot{P}_b^{Int} is still very useful: together with the measurement of q , it will eventually allow (with the assumption of the correctness of GR) a very precise estimate of the system masses and a precise calibration of the mass-radius relation for WDs.

ACKNOWLEDGMENTS

We are grateful to Julia Deneva for helping with many observations, to Arun Venkataraman for help in managing the large data sets resulting from this project year after year, Hector Hernández and the Arecibo operators for helping us optimize scheduling and usage of telescope time and Marten van Kerkwijk for useful comments and suggestions. We also thank Paul Demorest, Rob Ferdman, David Nice and Don Backer for permission to use the ASP to check the accuracy of our timing. PF and JPWV gratefully acknowledge the financial support by the European Research Council for the ERC Starting Grant BEACON under contract no. 279702. GE-F wishes to thank the Max-Planck-Institut für Radioastronomie for its kind hospitality during part of this work. He was also in part supported by the ANR grant 'THALES'. During most of this work JPWV was supported by the European Union under Marie Curie Intra-European Fellowship 236394. Pulsar research at UBC is supported by an NSERC Discovery Grant. Arecibo Observatory's William Gordon Telescope is a facility of the NSF. During this work it was operated through a cooperative agreement with Cornell University; it is now operated by SRI/USRA and Universidad Metropolitana. The Parkes Observatory is part of the Australia Telescope which is funded by the Commonwealth of Australia for operation as a National Facility managed by CSIRO. The WSRT is operated by ASTRON (Netherlands Foundation for Research in Astronomy) with support from The Netherlands Foundation for Scientific Research NWO. We would like to thank the referee, Thibault Damour, for constructive and detailed comments, which helped to improve the manuscript.

REFERENCES

- Alsing J., Berti E., Will C., Zaglauer H., 2012, Phys. Rev. D., 85, 064041
 Antoniadis J., van Kerkwijk M. H., Koester D., Freire P. C. C., Wex N., Tauris T. M., Kramer M., 2012, MNRAS, in press (doi:10.1111/j.1365-2966.2012.21124.x) (Paper I, this issue)
 Babichev E., Mukhanov V., Vikman A., 2008, J. High Energy Phys., 0802, 101
 Babichev E., Deffayet C., Esposito-Farèse G., 2011, Phys. Rev. D., 84, 061502
 Bassa C. G., van Kerkwijk M. H., Koester D., Verbunt F., 2006, A&A, 456, 295
 Bekenstein J. D., 2004, Phys. Rev. D., 70, 083509. [Erratum-ibid., D 71, 069901 (2005)]
 Bekenstein J. D., Sagi E., 2008, Phys. Rev. D., 77, 103512
 Bertotti B., Iess L., Tortora P., 2003, Nat, 425, 374
 Bhat N. D. R., Bailes M., Verbiest J. P. W., 2008, Phys. Rev. D., 77, 124017
 Brans C., Dicke R. H., 1961, Phys. Rev., 124, 925
 Bruneton J.-P., 2007, Phys. Rev. D., 75, 085013
 Bruneton J.-P., Esposito-Farèse G., 2007, Phys. Rev. D., 76, 124012
 Cordes J. M., Lazio T. J. W., 2001, ApJ, 549, 997
 Damour T., 2009, in Colpi M., Casella P., Gorini V., Moschella U., Possenti A., eds, Astrophys. Space Sci. Libr. Vol. 359, Physics of Relativistic Objects in Compact Binaries: from Birth to Coalescence. Springer, Berlin, p. 1
 Damour T., Deruelle N., 1985, Ann. Inst. Henri Poincaré, Phys. Théor., 43, 107
 Damour T., Deruelle N., 1986, Ann. Inst. Henri Poincaré, Phys. Théor., 44, 263
 Damour T., Esposito-Farèse G., 1992, Class. Quantum Grav., 9, 2093
 Damour T., Esposito-Farèse G., 1993, Phys. Rev. Lett., 70, 2220
 Damour T., Esposito-Farèse G., 1996a, Phys. Rev. D., 53, 5541
 Damour T., Esposito-Farèse G., 1996b, Phys. Rev. D., 54, 1474
 Damour T., Esposito-Farèse G., 1998, Phys. Rev. D., 58, 042001
 Damour T., Taylor J. H., 1991, ApJ, 366, 501
 Damour T., Gibbons G. W., Taylor J. H., 1988, Phys. Rev. Lett., 61, 1151
 Deller A. T., Verbiest J. P. W., Tingay S. J., Bailes M., 2008, ApJ, 685, L67
 Demorest P. B., 2007, PhD thesis, University of California, Berkeley
 Dowd A., Sisk W., Hagen J., 2000, in Kramer M., Wex N., Wielebinski R., eds, ASP Conf. Ser. Pulsar Astronomy – 2000 and Beyond, IAU Colloquium 177. Astron. Soc. Pac., San Francisco, p. 275
 Eardley D. M., 1975, ApJ, 196, L59
 Eddington A., 1923, The Mathematical Theory of Relativity. Cambridge Univ. Press, Cambridge
 Edwards R. T., Hobbs G. B., Manchester R. N., 2006, MNRAS, 372, 1549
 Fierz M., 1956, Helv. Phys. Acta, 29, 128
 Folkner W. M., Williams J. G., Boggs D. H., 2008, JPL Planetary and Lunar Ephemeris DE 421, Technical Report IOM 343R-08-003, NASA/Jet Propulsion Laboratory
 Freire P. C. C., Wex N., 2010, MNRAS, 409, 199
 Gonzalez M. E. et al., 2011, ApJ, 743, 102
 Hobbs G. B., Edwards R. T., Manchester R. N., 2006, MNRAS, 369, 655
 Hofmann F., Müller J., Biskupek L., 2010, A&A, 522, L5
 Jacoby B. A., 2005, PhD thesis, California Institute of Technology, California, USA
 Jacoby B. A., Hotan A., Bailes M., Ord S., Kuklarni S. R., 2005, ApJ, 629, L113
 Jacoby B. A., Bailes M., Ord S. M., Knight H. s., Hotan A. W., 2007, ApJ, 656, 408
 Jordan P., 1959, Z. Phys., 157, 112
 Karuppusamy R., Stappers B., van Straten W., 2008, PASP, 120, 191
 Kaspi V. M., Tauris T., Manchester R. N., 1996, ApJ, 459, 717
 Kramer M. et al., 2006, Sci, 314, 97
 Lange C., Camilo F., Wex N., Kramer M., Backer D., Lyne A., Doroshenko O., 2001, MNRAS, 326, 274
 Laskar J., Fienga A., Manche H., Kuchynka P., Le Poncin-Lafitte C., Gaspineau M., 2009, BAAS, 41, 881
 Lasky P. D., Sotani H., Giannios D., 2008, Phys. Rev. D., 78, 104019
 Lazaridis K. et al., 2009, MNRAS, 400, 805
 Lorimer D. R., Kramer M., 2005, Handbook of Pulsar Astronomy. Cambridge Univ. Press, Cambridge
 Milgrom M., 1983, ApJ, 270, 365
 Motz L., 1952, ApJ, 115, 562
 Nice D. J., Taylor J. H., 1995, ApJ, 441, 429
 Nice D. J., Splaver E. M., Stairs I. H., Löhmer O., Jessner A., Kramer M., Cordes J. M., 2005, ApJ, 634, 1242
 Nice D. J., Stairs I. H., Kasian L. E., 2008, in Bassa C., Wang Z., Cumming A., Kaspi V. M., eds, AIP Conf. Ser. Vol. 983, 40 Years of Pulsars: Millisecond Pulsars, Magnetars and More. Am. Inst. Phys., New York, p. 453
 Nordtvedt K., 1990, Phys. Rev. Lett., 65, 953
 Riess A. G. et al., 2009, ApJ, 699, 539
 Sanders R. H., 1997, ApJ, 480, 492
 Shapiro I. I., 1990, in Ashby N., Bartlett D. F., Wyss W., eds, Proc. 12th Int. Conf. General Relativity and Gravitation. Cambridge Univ. Press, Cambridge, p. 313

- Shklovskii I. s., 1970, *SvA*, 13, 562
 Smarr L. L., Blandford R., 1976, *ApJ*, 207, 574
 Stairs I. H., Thorsett S. E., Taylor J. H., Wolszczan A., 2002, *ApJ*, 581, 501
 Taylor J. H., 1992, *Philos. Trans. R. Soc. Lond.*, A 341, 117
 Verbiest J. P. W., Lorimer D. R., McLaughlin M. A., 2010, *MNRAS*, 405, 564
 Verbiest J. P. W. et al., 2008, *ApJ*, 679, 675
 Verbiest J. P. W. et al., 2009, *MNRAS*, 400, 951
 Weisberg J. M., Nice D. J., Taylor J. H., 2010, *ApJ*, 722, 1030
 Will C. M., 1993, *Theory and Experiment in Gravitational Physics*. Cambridge Univ. Press, Cambridge
 Will C. M., 2006, *Living Rev. Relativ.* 9, 3 (<http://www.livingreviews.org/lrr-2006-3>)

APPENDIX A: CONSTRAINING THE MASS LOSS OF THE WD COMPANION

The mass loss of the companion, \dot{M}_c , can be constrained by assuming (safely) that the energy driving the process comes from the pulsar. Its rotational energy loss is given by $\dot{E} = -I_p \Omega_p \dot{\Omega}_p = 4\pi^2 I_p \dot{P}_{\text{int}} P^{-3} = 4.4 \times 10^{33} \text{ erg s}^{-1}$, where \dot{P}_{int} is its intrinsic spin-down (which is calculated from the observed spin-down after taking into account kinematic effects; see Section 3.2), $I_p \sim 10^{45} \text{ g cm}^2$, its moment of inertia, and Ω_p , its angular velocity. Some of this radiated energy impacts the WD; its maximum occurs when the pulsar is beaming all the power right on the orbital plane, in which case the WD intercepts a fraction given by $f = 2R_c/(2\pi a)$, where R_c is the WD companion radius, $0.037 R_\odot$ (see Paper I) and $a = xc(q + 1)/\sin i$ is the orbital separation. This then provides the escaping particles with a velocity v_0 such that through conservation of energy

$$\frac{1}{2} \dot{M}_c v_0^2 < \dot{E} \frac{R_c}{\pi a} \Rightarrow \dot{M}_c < 2.60 \times 10^{-23} \text{ s}^{-1} \left(\frac{v_0}{c} \right)^{-2} M_t, \quad (\text{A1})$$

where we express the mass loss rate as a fraction of the total mass of the system. To first approximation, this initial velocity has to be larger than the escape velocity from the surface of the WD, $v_e = \sqrt{2GM_c/R_c} = 1.37 \times 10^3 \text{ km s}^{-1} = 0.0046 c$; this immediately yields $\dot{M}_c/M_t < 1.2 \times 10^{-18} \text{ s}^{-1}$.

In what follows, we assume that the gas escapes from the WD equally in all directions. The matter density is then given by $\rho(r) = \dot{M}_c/[4\pi r^2 v(r)]$ and the electron density by

$$n(r) = \frac{\dot{M}_c}{4\pi r^2 X \mu_p v(r)}, \quad (\text{A2})$$

where r is the distance to the centre of the WD, μ_p is the proton mass and X is the number of nucleons per electron (1 for hydrogen and 2 for heavy elements). Therefore, for any particular density profile $n(r)$, the larger the plasma velocity, the larger is \dot{M}_c . As calculated below, for the latter to be of any practical significance in the present case, v_0 has to be at least of the order of a few per cent of the speed of light c . In this case the plasma would be little affected by the WD escape velocity and have a nearly constant velocity. This results in an upper limit for the density profile given by $n(r) = \dot{M}_c/(4\pi r^2 X \mu_p v_0)$. Therefore, the upper limit for the extra column density along the length l of the line of sight from the pulsar to Earth is given by

$$H = \int_{-r_p \cos \psi}^{\infty} n(r) dl = \frac{\dot{M}_c}{4\pi X \mu_p v_0} \frac{\psi}{r_p \sin \psi}, \quad (\text{A3})$$

where r_p is the distance between the pulsar and the WD, and ψ is the angle between the direction to the pulsar and the direction to the observer as seen from the WD, in such a way that $r = [(r_p \sin \psi)^2 + l^2]^{1/2}$. This equation is similar to equation (5) of Kaspi, Tauris & Manchester (1996).

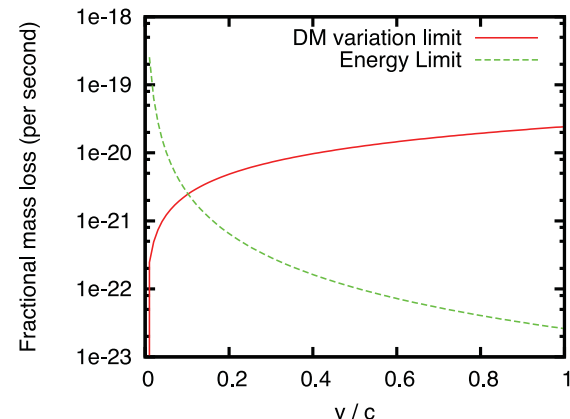


Figure A1. Upper limits for mass loss from the WD derived from upper limit of pulsar spin-down energy incident on the WD and 1σ upper limit on ΔDM . Their combination excludes a fractional mass loss larger than $2.5 \times 10^{-21} \text{ s}^{-1}$.

For a very low eccentricity orbit $r_p \simeq a$. For superior and inferior conjunction $\psi = \pi/2 + i$ and $\psi = \pi/2 - i$, respectively, therefore

$$\Delta H \equiv H_{\text{sup}} - H_{\text{inf}} = \frac{1}{2\pi} \frac{\dot{M}_c}{X \mu_p v_0} \frac{i}{a \sin i}. \quad (\text{A4})$$

Dividing by the total mass of the binary $M_t = M_p + M_c$ we obtain

$$\begin{aligned} \frac{\dot{M}_c}{M_t} &= 2\pi v_0 X \frac{\mu_p}{M_c} \frac{xc \cot i}{i} \Delta H \\ &= 1.97 \times 10^{-16} \text{ s}^{-1} \left(\frac{v_0}{c} \right) \Delta DM. \end{aligned} \quad (\text{A5})$$

In this expression we use $\Delta H = \Delta DM \times 3.0857 \times 10^{18} \text{ cm pc}^{-1}$ to convert the column density to a DM, $X = 2$ as an upper limit for X and the x and i measured for this system (see Table 1). The DM variations for PSR J1738+0333 are displayed in the left-hand plot of Fig. 4. Fitting an equivalent of equation (A3) to these DMs (also displayed in the same plot) we obtain $\Delta DM = (0.24 \pm 1.09) \times 10^{-4} \text{ cm}^{-3} \text{ pc}$, which is basically consistent with no observed dispersive delays.

Using the upper limit represented by equation (A1) and the 1σ upper limit (84 per cent C. L.) for ΔDM in equation (A5) we obtain $\frac{\dot{M}_c}{M_t} < 2.5 \times 10^{-21} \text{ s}^{-1}$, which happens at a velocity of about $0.1 c$ (see Fig. A1). This is large enough for the velocity to be nearly constant as a function of r (equation A5) but small enough for the Newtonian expression for the kinetic energy (equation A1) to provide a good approximation.

It is possible that the gas is being ejected slowly compared to the pulsar wind, in which case it might be blown away from the pulsar by its wind, forming a highly anisotropic ‘cometary’ tail. In that case the low orbital inclination of this system would mean that the plasma emanating from the WD might avoid crossing the line of sight, producing no extra dispersive delays detectable at the Earth. In such a case we can only rely on the energy balance to constrain the mass loss, which at these low plasma velocities allows, in the extreme case discussed above, for very substantial mass loss. There are, however, other binary pulsars with companion WDs of similar mass like PSR J0751+1807 (Nice et al. 2005) and PSR J1909–3744 (Jacoby et al. 2005) that happen to be observed at much higher inclinations, and in no case is such a cometary tail ever observed.

This paper has been typeset from a TeX/LaTeX file prepared by the author.